Quantifying bone marrow adiposity and its genetic architecture from head MRI scans

Tobias Kaufmann[1,2] (corresponding)
Pål Marius Bjørnstad[3]
Martin Falck[3]
Kevin O´Connell[1]
Oleksandr Frei[1,4]
Ole A. Andreassen[1,5]
Lars T. Westlye[1,5,6]
Srdjan Djurovic[3,7]
Timothy Hughes[1,3] (corresponding)

1 Norwegian Centre for Mental Disorders Research, Division of Mental Health and Addiction, Oslo University Hospital & Institute of Clinical Medicine, University of Oslo, Oslo, Norway

2 Department of Psychiatry and Psychotherapy, Tübingen Center for Mental Health, University of Tübingen, Tübingen, Germany

[3] Department of Medical Genetics, Oslo University Hospital, Oslo, Norway

[4] Centre for Bioinformatics, Department of Informatics, University of Oslo, Oslo, Norway

[5] KG Jebsen Centre for Neurodevelopmental Disorders, University of Oslo, Oslo, Norway

[6] Department of Psychology, University of Oslo, Oslo, Norway

[7] NORMENT, Department of Clinical Science, University of Bergen, Bergen, Norway

@ Correspondence: Name: Tobias Kaufmann, PhD
Email: tobias.kaufmann@med.uni-tuebingen.de
Postal address: Department of Psychiatry and Psychotherapy, University of Tübingen, Calwerstraße 14, 72076 Tübingen
Telephone: +49 7071 29 82 311

@ Correspondence: Name: Timothy Hughes, PhD
Email: timothy.hughes@medisin.uio.no
Postal address: Department of Medical Genetics, Oslo University Hospital, 166 Kirkeveien, 0407 Oslo, Norway
Telephone: +47 99 16 18 18

Content type: Full paper

Abstract

Recent animal work has documented a two-way interconnection between calvarial bone marrow and the brain. Bone marrow adiposity may therefore have direct implications for brain health, yet the lack of *in vivo* studies in humans limits our understanding of such interplay. Here, we exploit large magnetic resonance imaging (MRI) datasets to study bone marrow adiposity and its association with brain and body traits. We trained an artificial neural network to localise calvarial bone marrow in T1-weighted 3T MRI head scans. Validation in two independent samples confirmed high accuracy of our approach to semi-quantitatively measure calvarial bone marrow adiposity *in vivo*. Our analyses revealed sex-dimorphic age trajectories in line with earlier work from non-calvarial bone marrow. Next, we studied the genetic architecture of the calvarial bone marrow and revealed its high heritability in single-nucleotide polymorphism and twin data. We identified 41 genetic loci significantly associated with the calvarial bone marrow, including a sex-specific genetic effect of the estrogen receptor locus. By integrating mapped genes with existing bone marrow single-cell RNA sequencing data, we revealed patterns of adipogenic lineage differentiation and lipid loading. Finally, we identified significant genetic correlation with several heritable human traits, including general cognitive ability and Parkinson's disease. Our method for quantifying calvarial bone marrow adiposity from MRI head scans enables a significant advance in our understanding of the genetic and cellular drivers of bone marrow adiposity in humans. This contributes to the groundwork needed to elucidate its function and creates an opportunity to study its effects on other organs such as bone, blood, and brain.

Introduction

Bone marrow (BM) is a tissue located within trabecular bone which produces the cellular components of blood. Beginning in childhood, it undergoes a radical conversion from red to yellow adipose marrow[1] which begins in the limbs, but progresses more slowly in the flat bones of the axial skeleton[2]. By middle-age, BM adipose tissue accounts for 50-70% of total BM volume in healthy humans[3]. Men have higher bone marrow adiposity (BMA) than women, but post-menopausal women experience a rapid rise in BMA[4]. The biological causes and consequences of this phenomenon are poorly understood. It is established that BM fat has a distinct function to white and brown adipose tissue depots[5,6], but a precise definition of that function and the evolutionary reason for the sex-dimorphism remain elusive. What is known is that BM adipocytes and bone-forming osteoblasts both result from the bifurcating differentiation of mesenchymal stem cells in the BM niche and this lies at the root of the connection between BMA and osteoporosis[7–9]. Crucially, BM adipocytes have also been shown to affect the hematopeoitic microenvironment[10].

Magnetic resonance imaging (MRI) scans of the head are primarily thought of as a powerful non-invasive tool for investigating the structure and function of the human brain, but these scans also contain imaging information about other organs, such as bone marrow (BM). The calvarial bones contain a BM layer of approximately 600 cm^2 which is several millimetres thick[11,12] and has recently been shown to be connected to the meninges by direct vascular channels through the inner table of the calvarium[13]. These channels transport cerebrospinal fluid from the subarachnoid space to the cranial BM via a perivascular route[14,15] and myeloid blood cells travel in the opposite direction[13,16,17]. Thus, there is a clear potential for the state of calvarial BM to directly affect the brain.

BMA levels can be semi-quantitatively measured in T1-weighted MRI scans due to the greater signal intensity of fat[18–20]. Most large neuroimaging cohorts have acquired such data, but have concentrated on the brain image, thus MRI head scans present a hitherto unexplored opportunity to address three unresolved aspects of bone marrow biology. First, to quantify *in vivo* at population-scale BMA characteristics, such as age trajectory and sex-dimorphism, and its relationship to other traits, such as bone mineral density (BMD). Second, to estimate BMA's heritability and genetic architecture which are likely common to the marrow of all bones. Third, to determine whether the adiposity of calvarial BM, that envelops the neocortex and has direct channels to it, has any detectable effect on it.

We developed an artificial neural network-based method for measuring BMA in the calvarial bones, and successfully validated it using several publicly available MRI resources. We then applied this method to head MRI scans from the *UK Biobank*[21] to extract information on BMA, its spatial distribution in the calvaria and model its main demographic determinants. The size of the sample (n=33,042) enabled us to conduct a well-powered genome-wide analysis (GWAS) to identify genes that are associated with BMA and, using a single-cell RNA sequencing (scRNAseq) dataset of BM mesenchymal cells, we gained insight into which genes drive differentiation into the adipogenic lineage and which drive lipid loading. Finally, we investigated genetic overlap between BMA and twelve brain and body traits.

Results

Localisation of calvarial BM in head MRI scans

Our procedure for localising the BM and measuring its intensity involved 1. identifying the skin surface of the head, 2. identifying the calvarial part of the head using the top of the cerebellum and the accumbens as reference points, 3. for each point of the calvarial surface extracting an intensity array 25 mm into the skull (each layer is 0.5 mm thick), and 4. applying an artificial neural network to identify which layers of the intensity array correspond to BM (Figure 1). This network has 50 input nodes, 3 internal layers, and 6 output nodes (upper and lower bounds of outer table, BM, inner table). We trained this network on data from a simulation which incorporates the natural intra- and inter-individual variation in thickness and intensity of the relevant anatomical structures (Figure 1A, S1). Using the network's estimation of the localisation of the BM within the intensity array of a datapoint, we averaged these intensities to obtain the intensity for the datapoint, and then averaged these across all datapoints of the calvarium to produce the global BMA measure for the scan.

Procedure validation on simulated data

We evaluated the performance of the neural network on simulated data using two metrics (Figure 1B): 1. the overlap between the predicted and the true BM location, and 2. the ratio between the predicted intensity of the BM and the true intensity of the BM. The median overlap between the predicted BM and the true BM in the simulated dataset was 0.76 with the lowest value (0.4) obtained in calvaria with a thin bone and the highest value (0.88) obtained in calvaria with thick bone. Poor overlap (below 0.7) was almost only observed in the thinnest bone and is explained by the fact that, when the BM part of the bone is only a few layers thick (1 layer = 0.5 mm), an error by one layer will inevitably lead to a substantial fall in overlap. However, this did not result in a corresponding fall in the ratio of the predicted intensity of BM to its true intensity, because the typical BM intensity was only marginally higher than the neighbouring bone intensity. This property of the typical relative intensities of these anatomic structures also explained why the intensity ratio at high overlap is not centred on 1: any misidentification of cortical bone as BM, will typically result in an underestimate of true BM intensity (Figure S2). The neural network performed well and intensity ratios were in the range 0.9-1.1 for the vast majority of head types (Figure S3). It was only for heads with thin bone and either very high or very low BM intensity that we observed intensity ratios below or above this range (Figure S3B). Variation in subcutaneous fat thickness had no systematic impact on the performance (Figure S3C).

Procedure validation on real data and heritability estimate

The procedure also performed well on real data. We first tested a dataset from the *Consortium for Reliability and Reproducibility*[22] consisting of 30 individuals that were scanned 10 times each at 3-day intervals. The scans passing quality control displayed mean intensity of the outer table and BM at the levels that we would expect (Figure 1D): very low variation between scans of the same individual, outer table intensities centred on similar values with low variation across individuals, BM intensity always higher than outer table intensity, and high variation of BM intensity between individuals, but little within individuals. These scans were also inspected visually to verify that structure boundaries were correctly identified. Figure S4 provides examples of network performance in data of individuals with different levels of subcutaneous fat thickness, bone marrow adiposity, bone thickness.

The monozygotic (MZ) twin data from the *Human Connectome Project* cohort[23] (Figure 1E) provided a second validation of the procedure through the high concordance in mean BM signal intensity between MZ twins, 0.91 in male pairs and 0.82 in female pairs. Further, using

the data on the same-sex MZ and DZ twin pairs, we showed that BMA has an estimated broad-sense heritability of 91% in males and 60% in females (Table S1). We estimated a strong influence of environmental factors in females, one of which is highly likely to be estrogen levels as these vary widely between women of such a cohort of child-bearing age, with particularly large changes during pregnancy when estrogen levels are orders of magnitude higher, and the common use of estrogen-based contraceptives.

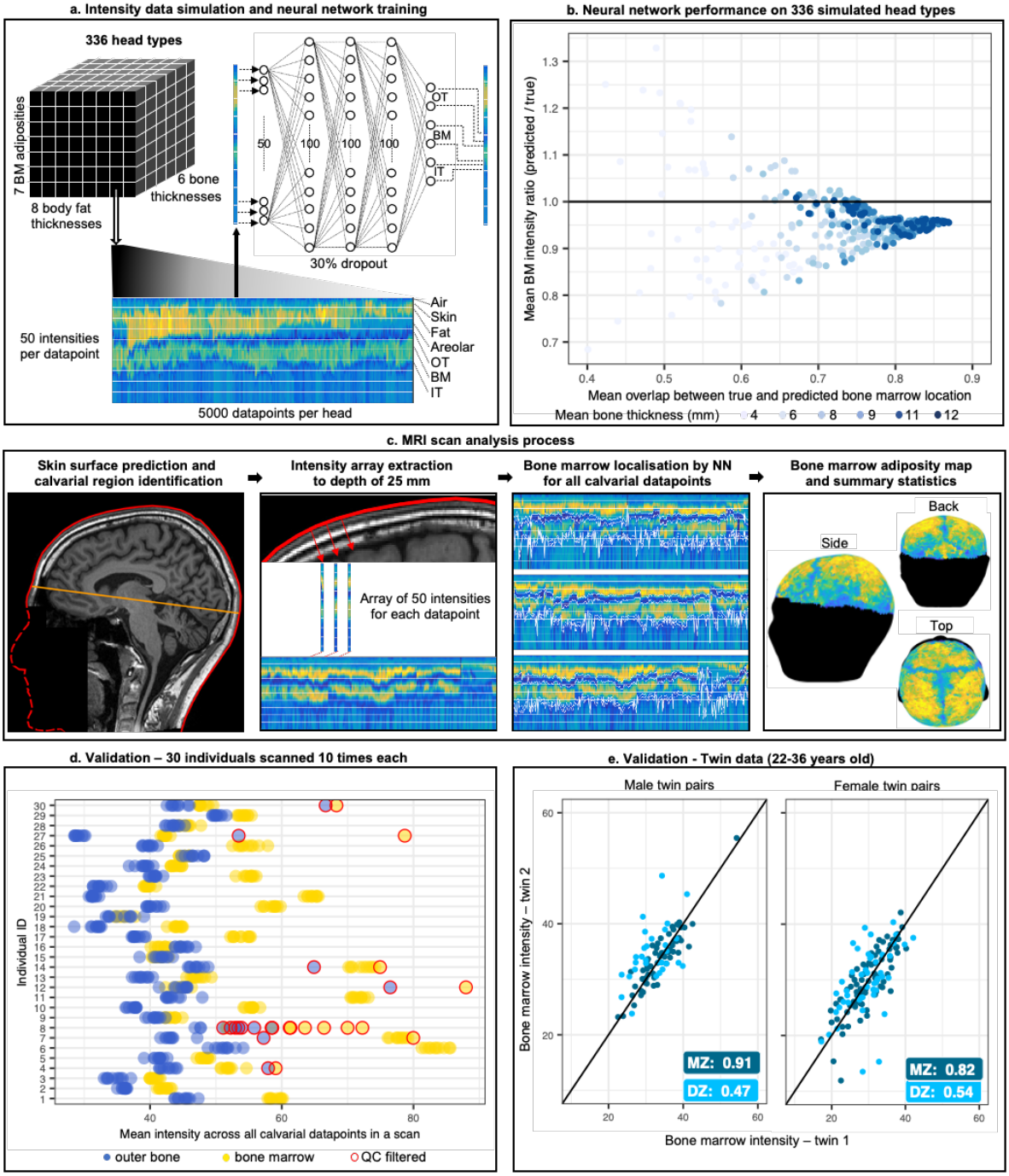

Figure 1: Overview of the artificial neural network training, application, and validation. **a**. The data used for training the network were generated by simulating 336 different head types where a head type is defined by mean bone thickness, mean BM intensity and mean body fat thickness. There are 5000 datapoints per head each with 50 intensities per datapoint. OT: outer table, IT: inner table, BM: bone marrow **b.** We evaluated the performance of the neural network using two metrics: 1. the overlap between the predicted and the true BM location (defined by the simulation), and 2. the ratio between the predicted signal intensity of the BM and the true intensity of the BM.

c. Illustration of the process of extracting the intensity arrays from the MRI scan, localising the BM, and computing its intensity.
d. The algorithm was validated on a real dataset consisting of 30 individuals that were scanned 10 times each at 3-day intervals. For each scan, we computed the intensity of the outer bone (blue) and of the BM (yellow) which displayed high concordance across scans of the same individuals. The quality control measures correctly identified scans not producing reliable measures (13 of 300, 11 of which fail due to too few datapoints).
e. Application of the algorithm to a cohort of monozygotic and same-sex dizygotic twins. Correlation in BMA between twin pairs in coloured boxes.

The calvarial BMA phenotype

In the 16,140 male and 16,902 female white British individuals from the *UK Biobank* for which head imaging data is available, we observed that calvarial BMA had strongly sex-dimorphic features. Males had a higher mean BMA than females (Figure 2A) and showed no increase at the group level in BMA levels in the age range covered by the biobank sample (45 to 82 years) implying that the rise in BMA must have occurred earlier in life (Figure 2B). In females the BMA level was highly dynamic in this age range increasing by 50% in the same age interval and thereby reaching male levels at age 70. Hormone replacement therapy (HRT) was used at some point in life by 38% of the women in the study and this therapeutic intervention slowed the rise in BMA, resulting in average BMA levels for treated women that did not exceed the level of males at age 80.

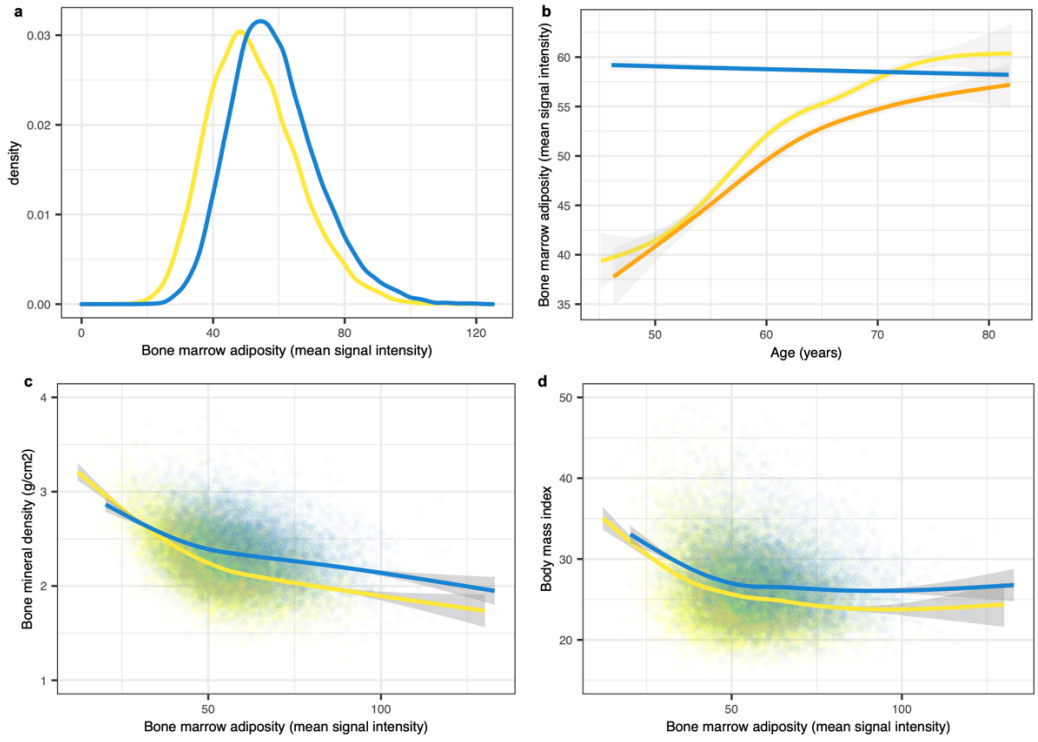

Figure 2: The calvarial BMA phenotype
a. BM intensity distribution in males (blue) and females (yellow)
b. BMA age trajectories for males and females. Males in blue and females in yellow (never HRT) and orange (ever HRT). The effects of age and HRT on female BMA levels were both statistically significant (p-value < 2.0E-16)
c. Sex-dimorphic relationship between BMA and calvarial bone mineral density.
d. Relationship between BMA and BMI.

Fitted lines in B, C, and D were computed using a general additive model and shading represents 95% confidence intervals.

BM adipocytes and osteoblasts differentiate from the same mesenchymal progenitor cells and this would appear to drive the known negative correlation between BMA and bone mineral density (BMD). We observe this in our data (Figure 2C – 14,262 males and 14,831 females). This relationship is also dimorphic with females displaying a lower level of calvarial BMD for a given level of BMA. Further, the size of the female BMD deficit increases as BMA levels rise (a similar pattern is observed with BMI in Figure 2D). We quantify the determinants of calvarial BMD by linear regression (Table S2). These regressions confirm the known effects of age and sex, and that the effect of BMA on BMD is about twice as large in females relative to males. Our regression results suggest that most of the effect of HRT on BMD is mediated by its effect on BMA (Table S2) since: 1. the statistical significance of HRT as an explanatory variable for BMD disappears when BMA is included as an explanatory variable in the regression and 2. the R^2 of the regression increases by a factor of 4 to 30%.

Genetic architecture

The strong twin-based heritability of BMA emphasised the importance of a genome-wide association study (GWAS) of the trait. We used the *UK Biobank* cohort (Table S3) and performed sex-specific covariate regression prior to separate discovery GWASs on males (n=16,140) and females (n=16,902). We found them to have low genomic inflation (Figure 3A and Table S4) and to be significantly genetically correlated (Rg=.94, P=6e-27, Figure 3B), allowing us to combine these samples to perform a joint discovery GWAS across males and females (n=33,042). Further, we performed an independent replication GWAS (n=4,958) on non-white British males and females.

SNP-based heritability (h^2_{SNP}) estimated using linkage disequilibrium score regression confirmed significant heritability of the joint discovery GWAS, (h^2_{SNP} = 31.5%) (Table S4). We identified 168 genome-wide significant independent SNPs (P<5e-8), corresponding to 41 independent genomic loci (Table S5). The replication GWAS also displayed significant heritability (h^2_{SNP} = 28.6%). Out of the 168 significant discovery SNPs, 62% replicated at P<.05, and 39% of the 41 lead SNPs replicated at P<.05 (Table S6). One locus replicated at genome-wide significance (P<5e-8). Furthermore, 92.7% of the lead SNPs of the discovery sample showed same effect direction in the replication sample (Table S5).

Figure 3C depicts genes mapped from the 41 loci associated with the calvarial BMA. The most significant top lead SNP was located in the WNT16 gene (P=2.6e-143), which is also the top hit in BMD GWAS[24,25] (Figure S9). The ESR1 locus displayed a notable sex dimorphic pattern (Figure S10). In females, the top lead SNP overlapped the ESR1 gene, but another lead SNP overlapped the neighbouring CCDC170 gene. In males, the signal in ESR1 was absent, but a genome-wide significant signal was located in the CCDC170 gene, suggesting that the ESR1 gene might not be the only source of an association signal in this locus.

A comparison of the male and female effect sizes of the top lead SNPs of each locus revealed 6 loci in which there is a more than two-fold difference between the sexes (loci 10, 18, 26, 30, 32, 37 in Table S5). In all cases, it is the male effect size that is larger. Further, each locus is genome-wide significant in males, but not in females, thus suggesting that these loci may be genetic drivers of the sex-dimorphism.

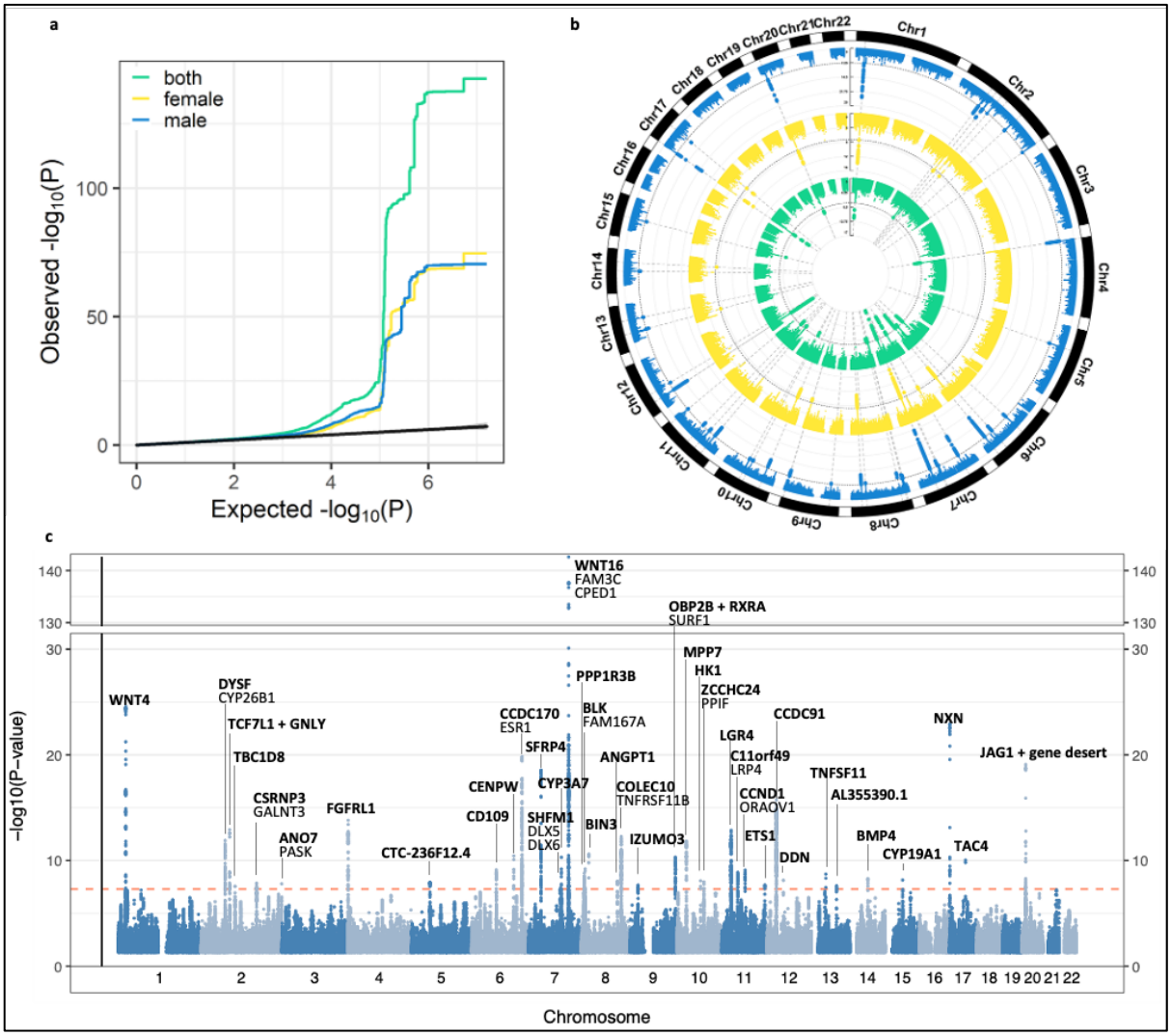

Figure 3: BMA genome-wide significant loci

a. QQ-plot of p-values for the male, female and joint discovery GWAS

b. Comparison of male (outer), female (middle), and joint (inner) discovery GWAS significant loci.

c. Manhattan plot of the 41 genome-wide significant loci in the joint discovery GWAS named after gene closest to the top lead SNP (bold). Other genes in each locus for which genome-wide significant SNPs were eQTLs, are listed below the closest gene. Three loci were closely adjacent to another more significant locus and are marked "+". SNPs with $p < 0.05$ not plotted.

Gene expression in BM mesenchymal stem cell differentiation

Mesenchymal stem cells of the bone marrow niche commit to either the adipogenic or the osteogenic lineage (Figure 4A) and both the number committing to the adipogenic lineage and their level of lipid-loading influences the total level of BMA. We made use of an existing scRNAseq dataset of BM mesenchymal lineage cells[26] to study variation in the expression of BMA-associated genes as cells differentiate (Figure 4B). For any given gene, the percent of cells expressing a gene was relatively stable across different cell types. However, the mean scaled expression varied considerably between differentiation stages and the clustering of expression profiles revealed that most genes fall into one of the two largest groups of profiles: either genes with their peak of expression at the lineage commitment stage (LMP and LCP) or within the adipogenic lineage (MALP). It was also noteworthy that the genes

peaking in MALPs mostly showed low expression prior to that stage. This differed from the ramping up observed in mesenchymal progenitors and LCPs. Only one of the closest genes saw their peak of expression in osteoblasts, but it was unexpected to observe that 6 of the closest genes see a strong peak in osteocytes. It remains to be investigated whether the closest gene might not be the source of the association or whether gene expression in osteocytes may have an influence on BMA.

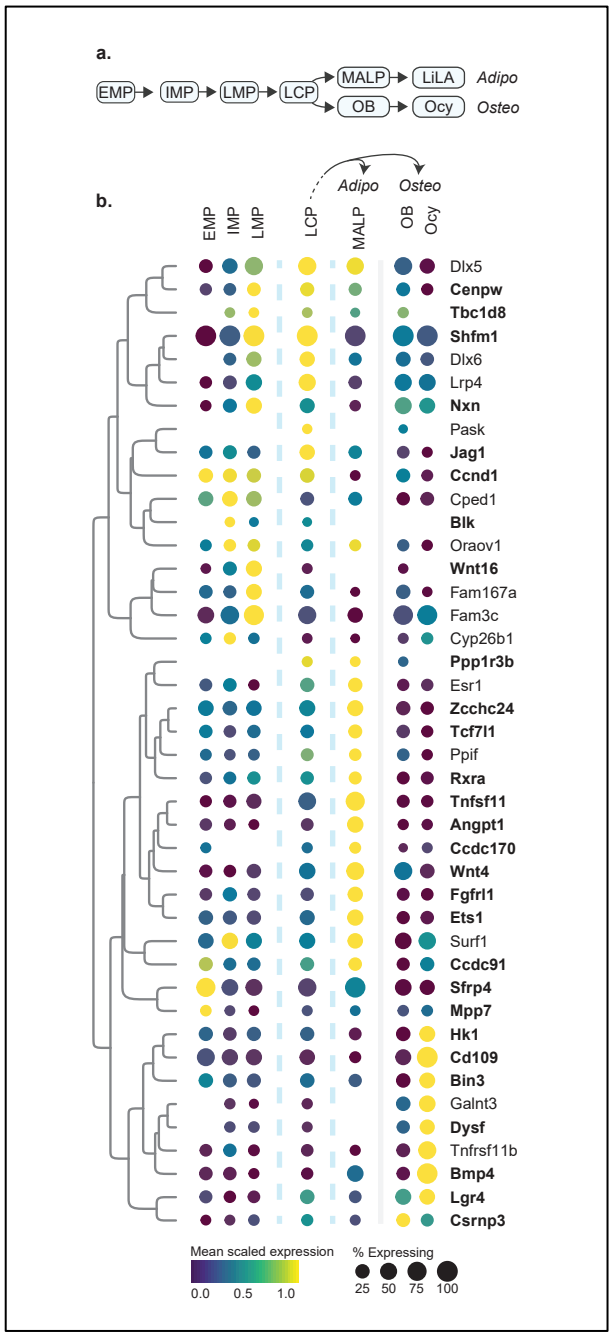

Figure 4: Gene expression in mesenchymal lineage cells of mouse BM.
a. The differentiation of BM mesenchymal cells. Early (EMP), intermediate (IMP), and late mesenchymal progenitors (LMP). Lineage committed progenitors (LCP). Marrow adipogenic lineage precursor (MALP). Lipid-laden Adipocyte (LiLA). Osteoblast (OB). Osteocyte (Ocy).
b. A clustering of the gene expression profiles across cell types. Gene names are for mouse genes (these broadly match human gene names). Of the 40 genes which are closest to lead SNP for each locus, 28 had expression in the scRNAseq data (bold). LiLA expression data was not available in this dataset.

Genetic correlation and overlap

We investigated genetic correlation and overlap with 12 traits. We selected body traits (BMD, BMI, systolic and diastolic blood pressure, type-2 diabetes, coronary artery disease) that have a logical connection to BMA given the mesenchymal stem cells origin of BM adipocytes and their role in bone, fat, and vasculature[26]. For the brain, we selected traits reflecting cognition (general cognitive ability and educational attainment) and disorders that are prevalent in adulthood (insomnia, multiple sclerosis, Parkinson's disease, Alzheimer's disease) since it is primarily in adulthood that the adiposity of calvarial BM experiences a substantial change (Figure 2B).

We identified strong negative genetic correlations between BMA and both BMD and BMI, and more subtle global genetic correlations between BMA and Parkinson's disease, general cognitive ability, and educational attainment (Table 1). However, global genetic correlations lack the ability to assess genetic overlap in the presence of mixed effect directions. So, to better understand the genetic overlap between BMA and other traits of interest, we also applied MiXeR[27]. MiXeR uses trait polygenicity, defined as the number of trait-influencing variants required to explain 90% of SNP-based heritability, to model the number of shared trait-influencing-variants between two traits as well as the correlation within this shared component. MiXeR estimates that 99% of BMA trait-influencing variants are shared with BMD (497 of 500 variants), and that the correlation of this shared component is -0.95, indicating high genetic overlap with discordant effect. The proportion of BMA trait-influencing variants also estimated to influence general cognitive ability (0.57) and educational attainment (0.67) was lower than observed for BMD, but the correlations within their shared components were similarly large (COG = 0.93, EDU = 0.90). These patterns of high overlap and high effect correlation within this overlap are suggestive of vertical pleiotropy i.e. a molecular mechanism influencing one trait, that in turn influences a second trait.

In Parkinson's Disease, where we also estimated statistically significant genetic correlation with BMA, MiXeR estimates a strong negative correlation of effect sizes, but this is within a much lower percentage of BMA trait-influencing variants (14%), indicating that BMA's effect on Parkinson's Disease is less likely to be causal. Similarly, BMA displayed a high correlation of effect sizes (-0.69) with Type-2 diabetes but within a moderate overlap, and a low correlation of effect sizes with both systolic and diastolic blood pressure but with an overlap of 95%. These patterns are more indicative of horizontal pleiotropy (i.e. molecular mechanisms influencing multiple traits) than vertical pleiotropy.

Trait	Genetic correlation (LDSR)			Genetic overlap (MiXeR)				
	All subjects			Partitioning of causal variants Mean nb per partition			Overlap as fraction of all BMA causal variants	Corr. of effect sizes within overlap (s.e)
	r_g	*P*	*Q*	Unique to BMA	Overlap	Unique to trait		
Bone mineral density	-0.41	1.5E-22	1.8E-21	3	497	1471	0.99	-0.95 (0.05)
Body mass index	-0.20	9.3E-15	5.6E-14	NA*	NA*	NA*	NA*	NA*
Blood pressure systolic	-0.02	6.5E-01	6.8E-01	25	475	3921	0.95	-0.25 (0.05)
Blood pressure diastolic	-0.03	3.4E-01	4.1E-01	27	473	3541	0.95	-0.21 (0.04)
Coronary artery disease	-0.10	3.6E-02	7.2E-02	275	225	1140	0.45	-0.40 (0.11)
Type-2 diabetes	-0.07	6.5E-02	1.1E-01	361	139	752	0.28	-0.69 (0.16)
Insomnia	-0.05	2.1E-01	2.8E-01	248	252	8868	0.50	-0.45 (0.32)
Multiple Sclerosis	-0.02	6.8E-01	6.8E-01	474	26	86	0.05	0.45 (0.14)
Parkinson's disease	-0.15	1.7E-03	4.1E-03	432	68	844	0.14	-0.75 (0.14)
Alzheimer's disease	-0.13	9.2E-02	1.4E-01	485	15	52	0.03	-0.61 (0.24)
General cognitive ability	0.09	1.1E-03	3.3E-03	217	283	10802	0.57	0.93 (0.12)
Educational attainment	0.10	9.9E-05	4.0E-04	166	334	12855	0.67	0.90 (0.11)

Table 1: Genetic correlation and overlap of BMA with other traits

r_g: genetic correlation. *Q*-values are FDR corrected *P*-values. Genetic overlap: number of causal variants that overlap (i.e. are shared) between BMA and the second trait. Total number of estimated causal variants for a trait (i.e. explaining 90% of SNP heritability) is the sum of those unique to trait and overlap (large total is indicative of high polygenicity). NA*: The publicly available summary statistics of the BMI GWAS contained only 3.3M SNPs, it was thus not possible to apply the MiXeR method to this dataset. Sex-specific genetic correlations, standard errors for causal variant partitioning, and Akaike Information criterion values (Table S9). Blue highlighting for: genetic correlation $p < 0.01$, overlap fraction > 0.5, correlation of effect sizes within overlapping > 0.5 or < -0.5.

Discussion

The development of a method for localizing BM in MRI head scans enabled us to characterize calvarial BMA in several datasets and to quantify, *in vivo* and at population-scale, BMA's age trajectory, sex-dimorphism, and relationship to BMD. Further, through a well-powered GWAS, we identified the main genetic drivers of this phenotype and we observed significant genetic correlation and overlap with several traits, including Parkinson's disease and general cognitive ability.

Measuring BMA in MRI head scans

Calvarial BM has a number of features which make it particularly well-suited to the study of BMA. First, conversion to yellow BM is slower in the flat bones[28], such that sex-dimorphic trajectories are observable in middle-aged cohorts. Second, there are many large collections of MRI scans from which calvarial BMA can potentially be extracted. Finally, it has a simple "sandwiched" structure that we were able to model and then generate simulated calvaria which we use as training data for an artificial neural network Our validation procedures demonstrate that this automated BM localisation procedure delivers good performance on real data, even though it was trained on simulated data and analyses each datapoint independently of all others. A more sophisticated model, trained directly on annotated real data, may raise performance further, for example by improving the prediction of the lower bound of the BM. However, this would require a substantial manual annotation effort and would face the difficult challenge of distinguishing low-adiposity BM from calvarial bone. Both these issues are circumvented by our approach.

The calvarial BMA and BMD phenotypes

The sex-dimorphic nature of BM adiposity is qualitatively well-established[4], but has not previously been quantified in a large human cohort. Males have a high and stable average level of BMA over the covered age range (45 to 82 yo), indicating that the dynamic male phase occurs earlier in life. The youngest females in our sample have a low level which ramps at a constant rate from the beginning to the end of the range with HRT significantly reducing the rate of increase. Interestingly, however, by the age of 70 (for women not using HRT), female BMA has risen to the same level as males. It appears highly likely that the menopause and the accompanying drop in natural estrogen levels is part of what drives the rise in BMA levels and that estrogen treatment can delay the rise. We emphasise that these trajectories are for calvarial BM and are most probably different in profile and levels to other BM, since it is known that flat bones convert later and perhaps less completely than the appendicular bones. However, the nature of the sex-dimorphism and the effect of estrogen is likely shared with other BM.

Women at risk of osteoporosis are often prescribed HRT in order to improve BMD. Our regression results (Table S2) indicate that the effect of HRT on BMD is mostly mediated by its effect on BMA. Further, we suspect that the effect of BMA on BMD may be underestimated given that the prescription of HRT is biased towards women with low BMD and high BMA. Future studies, including information on why HRT was prescribed and for how long, may use our BMA quantification method to further detail this important relationship.

BMA heritability estimates

Our findings showed that male SNP heritability (43%) is half the broad-sense heritability (91%). In females, SNP heritability is only 23% which is low relative to men and relative to the broad-sense heritability of 60%. Since the vast majority of women in the *UK Biobank* sample have probably not reached their ultimate BMA levels, we suspect that the genetic effects on the phenotype may be underestimated in this female GWAS sample. Despite these features of the sample and its relatively modest size, we do observe good genetic correlation between the sexes of the discovery sample (Figure 3b) and cross-ethnic replication in a limited sample of 4,958 individuals. Based on these GWAS results, MiXeR estimates that BMA has approximately 500 causal variants, indicating low polygenicity relative to a typical polygenic trait such as BMD, which we estimated to have approximately two thousand causal variants.

The high broad-sense heritability estimates indicate that environmental effects on BMA are limited relative to genetics. However, a limitation of our broad-sense heritability estimates is that the age range of the twin dataset is much younger than the *UK Biobank* dataset from which we compute SNP heritability. This is particularly relevant for females, first because fluctuations in estrogen levels are substantial during child-bearing age due to pregnancy and contraception, and second because females only reach their ultimate BMA level between the ages of 70 and 80 (the upper end of the age range). Both the broad-sense and SNP heritability estimates should therefore be interpreted with caution for females.

Genetic correlation and overlap with other traits

We selected 6 body and 6 brain traits for which we computed genetic correlation, and obtained significant results for BMD, BMI, Parkinson's disease, general cognitive ability and educational attainment. Genetic correlation has two limitations. First, it tends to underestimate the true correlation in the case of mixed effects and, second, it provides no indication of whether the relationship between the traits is driven by horizontal or by vertical pleiotropy. MiXeR estimates the causal variants for each trait and thereby can estimate the overlapping fraction as well as the correlation of effect within this set. A high overlap of BMA causal variants with those of the other trait and a high correlation of effects within this set is suggestive of causal effect (vertical pleiotropy). Only 3 of the 12 traits displayed a clear combination of such features. One of these is BMD, which can be considered as a positive control since the BMA and BMD traits are known to be negatively correlated and the bifurcating differentiation of mesenchymal stem cells provides a causal cellular mechanism for this relationship between traits. The other two traits are educational attainment and general cognitive ability. Since these are two highly correlated traits[29], a high overlap and correlation of genetic effects for both traits with BMA strengthens the evidence for a possible causal effect of BMA on cognition (Table 1).

GWAS results and differentiation of mesenchymal progenitors

Previous studies of mesenchymal cell differentiation in animal and cell models have pointed towards the Wnt/β-catenin signaling pathway being an important determinant of BMA[30]. Our large-scale phenotyping of BMA in a human cohort enabled us to perform a hypothesis-free

quantification of its genetic architecture which confirmed the strong effect of genes related to this pathway, including WNT16[31], WNT4[32], NXN[33]. Further, we found associations in genes (BMP4[34,35], DLX5[9,36], LGR4[37]) or close paralogs of genes (LRP4/LRP5[38], SFRP4/SFRP1[39]) that were known to specifically influence adiposity. We also discovered and quantified the effect of many interesting novel loci, such as FGFRL1 which has a pleiotropic role in hypertension resistance and bone growth in giraffes[40]. The strong effects of the CCDC170/ESR1 and WNT16 loci (Table S5) were not unexpected given previous results from the BMD GWAS[25], but the pattern of the genetic signal illustrates the importance of fine mapping for these and other loci (Figures S9-10).

Recent scRNAseq studies of the BM niche have provided a comprehensive insight into BM cell types and the changes in gene expression during differentiation [41–43]. Zhong et al. focused specifically on mesenchymal lineage cells and produced a detailed transcriptomic profile of progenitor maturation and bifurcating differentiation into adipogenic and osteogenic lineages[26]. Interestingly, they identify a new non-proliferative cell type in the adipogenic lineage that does not contain lipid droplets (MALP: marrow adipogenic lineage precursors). In our clustering of GWAS genes according to their scRNAseq transcriptomic profiles, we find 17 genes which ramp expression in mesenchymal progenitors with the peak of expression occurring in LMP or LCP, and 16 genes with very low expression in mesenchymal progenitors and a distinct peak at the MALP stage. Since BMA is primarily determined by two potentially asynchronous processes, the number of adipocytes and the level of lipid-loading, this suggests that the first set (including WNT16) controls the bifurcation between the two main lineages, whilst the second set (including ESR1) controls MALPs further differentiation into lipid-laden adipocytes.

MALPs outnumber lipid-laden adipocytes by orders of magnitude in young mice and exist as pericytes and stromal cells that form a ubiquitous 3D network inside the marrow cavity[26]. Evidence points to this network playing pivotal roles in maintaining marrow vasculature[26], suppressing osteogenic differentiation[44], and probably also influencing hematopoiesis[10]. We tentatively speculate that calvarial MALPs may be involved in sensing perivascular flows of CSF from the meninges to the BM and in influencing the BM's hematopoietic response, and that this might be the basis of the observed genetic overlap between BMA and some cerebral traits.

Conclusion

Hitherto, the study of BMA, especially at the molecular level, has mostly been performed in mice or *in vitro*. Our development of a method for localising BM in head MRI scans unlocked a new and abundant source of BMA data, which enabled us to quantify at population-scale the key features of the BMA phenotype, including its age trajectory, sex-dimorphism, response to HRT treatment, and relationship to BMD. Through genetic analyses, we identified the main genetic determinants of BMA, including the loci which are likely to be driving the sex-dimorphism. Finally, we found intriguing genetic overlap between calvarial BMA and general cognitive ability, educational attainment, and Parkinson's disease, suggesting that calvarial BM adipocytes, probably through their effect on the hematopoetic niche, may influence brain health. Future studies can therefore build on our developments to study calvarial BMA and its impact on the brain in clinical populations.

Acknowledgements

We acknowledge the following funding sources. TK: RCN (276082, 323961). TH: RCN (295679). OAA: RCN (223273) and EU's H2020 RIA (grant 847776). LTW: EU H2020 ERC StG (Grant 802998); RCN (223273, 249795, 248238, 286838); the South-Eastern Norway Regional Health Authority (2014097, 2015044, 2015073, 2016083, 2018037, 2018076. 2019101). We would like to thank everyone involved with the collection and sharing of imaging and genetics data used in this study.

Analysis was performed on the TSD computer facilities, owned by the University of Oslo, operated and developed by the TSD service group at the University of Oslo, IT-Department (USIT) and on resources provided by UNINETT Sigma2 - the National Infrastructure for High Performance Computing and Data Storage in Norway.

Data availability

This research has been conducted using the *UK Biobank Resource*[45] (access code 27412), the *Human Connectome Project*[46], and data from Hangzhou Normal University as part of the data provided by the *Consortium for Reliability and Reproducibility*[22]. *Human Connectome Project* data was provided by the WU-Minn Consortium (Principal Investigators: David Van Essen and Kamil Ugurbil; 1U54MH091657) funded by the 16 NIH Institutes and Centers that support the NIH Blueprint for Neuroscience Research; and by the McDonnell Center for Systems Neuroscience at Washington University. We obtained GWAS summary statistics from the following consortia: Genetic Factors for Osteoporosis Consortium, Genetic Investigation of ANthropometric Traits, ICBP International Consortium for Blood Pressure, Diabetes Genetics Replication And Meta-analysis Consortium, Coronary Artery Disease Genome-wide Replication and Meta-analysis Consortium, Complex Traits Genetics Consortium, Social Science Genetic Association Consortium, International Multiple Sclerosis Genetics Consortium, International Parkinson Disease Genomics Consortium, Psychiatric Genomics Consortium. BMA GWAS summary statistics are available on the FUMA website (ID XXXX) *[made public upon acceptance]*

Code availability

All code and software needed to generate the results is available as part of public resources: LD score regression (https://github.com/bulik/ldsc), FUMA (https://fuma.ctglab.nl/), MiXeR (https://github.com/precimed/mixer), BM localisation (simulation, training, and model) *[made public upon acceptance.*

Author contributions

TH TK SD conceptualized the study.

TH TK PMB MF KOC performed the analysis.

TH TK PMB MF KOC drafted the manuscript.

All authors contributed to and approved the final version.

References

1. Moore, S. G. & Dawson, K. L. Red and yellow marrow in the femur: age-related changes in appearance at MR imaging. *https://doi.org/10.1148/radiology.175.1.2315484* **175**, 219–223 (1990).
2. Veldhuis-Vlug, A. G. & Rosen, C. J. Clinical implications of bone marrow adiposity. *J. Intern. Med.* **283**, 121–139 (2018).
3. Cawthorn, W. P. & Scheller, E. L. Editorial: Bone marrow adipose tissue: Formation, function, and impact on health and disease. *Front. Endocrinol. (Lausanne).* **8**, 112 (2017).
4. Griffith, J. F. *et al.* Bone marrow fat content in the elderly: A reversal of sex difference seen in younger subjects. *J. Magn. Reson. Imaging* **36**, 225–230 (2012).
5. Hardouin, P., Rharass, T. & Lucas, S. Bone Marrow Adipose Tissue: To Be or Not To Be a Typical Adipose Tissue? *Front. Endocrinol. (Lausanne).* **7**, 85 (2016).
6. Suchacki, K. J. *et al.* Bone marrow adipose tissue is a unique adipose subtype with distinct roles in glucose homeostasis. *Nat. Commun. 2020 111* **11**, 1–18 (2020).
7. Meunier, P., Aaron, J., Edouard, C. & Vignon, G. Osteoporosis and the replacement of cell populations of the marrow by adipose tissue. A quantitative study of 84 iliac bone biopsies. *Clin. Orthop. Relat. Res.* **80**, 147–154 (1971).
8. Justesen, J. *et al.* Adipocyte tissue volume in bone marrow is increased with aging and in patients with osteoporosis. *Biogerontology* **2**, 165–171 (2001).
9. Rauch, A. *et al.* Osteogenesis depends on commissioning of a network of stem cell transcription factors that act as repressors of adipogenesis. *Nat. Genet. 2019 514* **51**, 716–727 (2019).
10. Naveiras, O. *et al.* Bone-marrow adipocytes as negative regulators of the haematopoietic microenvironment. *Nat. 2009 4607252* **460**, 259–263 (2009).
11. Lillie, E. M., Urban, J. E., Lynch, S. K., Weaver, A. A. & Stitzel, J. D. Evaluation of Skull Cortical Thickness Changes With Age and Sex From Computed Tomography Scans. *J. Bone Miner. Res.* **31**, 299–307 (2016).
12. Law, S. K. Thickness and resistivity variations over the upper surface of the human skull. *Brain Topogr.* **6**, 99–109 (1993).
13. Herisson, F. *et al.* Direct vascular channels connect skull bone marrow and the brain surface enabling myeloid cell migration. *Nat. Neurosci.* **21**, 1209–1217 (2018).
14. Pulous, F. E. *et al.* Cerebrospinal fluid can exit into the skull bone marrow and instruct cranial hematopoiesis in mice with bacterial meningitis. *Nat. Neurosci. 2022 255* **25**, 567–576 (2022).
15. Mazzitelli, J. A. *et al.* Cerebrospinal fluid regulates skull bone marrow niches via direct access through dural channels. *Nat. Neurosci. 2022* 1–6 (2022) doi:10.1038/s41593-022-01029-1.
16. Cai, R. *et al.* Panoptic imaging of transparent mice reveals whole-body neuronal projections and skull–meninges connections. *Nat. Neurosci.* **22**, 317–327 (2019).
17. Cugurra, A. *et al.* Skull and vertebral bone marrow are myeloid cell reservoirs for the meninges and CNS parenchyma. *Science (80-.).* **373**, (2021).
18. Cordes, C. *et al.* MR-Based Assessment of Bone Marrow Fat in Osteoporosis, Diabetes, and Obesity. *Front. Endocrinol. (Lausanne).* **7**, 74 (2016).
19. Loevner, L. A., Tobey, J. D., Yousem, D. M., Sonners, A. I. & Hsu, W. C. MR Imaging Characteristics of Cranial Bone Marrow in Adult Patients with Underlying Systemic Disorders Compared with Healthy Control Subjects. *Am. J. Neuroradiol.* **23**, (2002).
20. Simonson, T. M. & Kao, S. C. S. Normal childhood developmental patterns in skull bone marrow by MR imaging. *Pediatr. Radiol. 1992 228* **22**, 556–559 (1992).

21. Sudlow, C. *et al.* UK Biobank: An Open Access Resource for Identifying the Causes of a Wide Range of Complex Diseases of Middle and Old Age. *PLOS Med.* **12**, e1001779 (2015).
22. Zuo, X. N. *et al.* An open science resource for establishing reliability and reproducibility in functional connectomics. *Sci. Data 2014 11* **1**, 1–13 (2014).
23. Glasser, M. F. *et al.* The Human Connectome Project's neuroimaging approach. *Nat. Neurosci. 2016 199* **19**, 1175–1187 (2016).
24. Koller, D. L. *et al.* Meta-analysis of genome-wide studies identifies WNT16 and ESR1 SNPs associated with bone mineral density in premenopausal women. *J. Bone Miner. Res.* **28**, 547–558 (2013).
25. Morris, J. A. *et al.* An atlas of genetic influences on osteoporosis in humans and mice. *Nat. Genet.* **51**, 258–266 (2019).
26. Zhong, L. *et al.* Single cell transcriptomics identifies a unique adipose lineage cell population that regulates bone marrow environment. *Elife* **9**, (2020).
27. Frei, O. *et al.* Bivariate causal mixture model quantifies polygenic overlap between complex traits beyond genetic correlation. *Nat. Commun. 2019 101* **10**, 1–11 (2019).
28. Chan, B. Y., Gill, K. G., Rebsamen, S. L. & Nguyen, J. C. MR Imaging of Pediatric Bone Marrow. *https://doi.org/10.1148/rg.2016160056* **36**, 1911–1930 (2016).
29. Savage, J. E. *et al.* Genome-wide association meta-analysis in 269,867 individuals identifies new genetic and functional links to intelligence. *Nat. Genet. 2018 507* **50**, 912–919 (2018).
30. Tencerova, M. & Kassem, M. The bone marrow-derived stromal cells: Commitment and regulation of adipogenesis. *Front. Endocrinol. (Lausanne).* **7**, 127 (2016).
31. Shen, J. *et al.* Effects of WNT3A and WNT16 on the Osteogenic and Adipogenic Differentiation of Perivascular Stem/Stromal Cells. *Tissue Eng. Part A* **24**, 68 (2018).
32. Zhang, Q. *et al.* Roles and action mechanisms of WNT4 in cell differentiation and human diseases: a review. *Cell Death Discov. 2021 71* **7**, 1–10 (2021).
33. Funato, Y. & Miki, H. Nucleoredoxin, a novel thioredoxin family member involved in cell growth and differentiation. *Antioxid. Redox Signal.* **9**, 1035–1057 (2007).
34. Bowers, R. R., Kim, J. W., Otto, T. C. & Lane, M. D. Stable stem cell commitment to the adipocyte lineage by inhibition of DNA methylation: role of the BMP-4 gene. *Proc. Natl. Acad. Sci. U. S. A.* **103**, 13022–13027 (2006).
35. Bowers, R. R. & Lane, M. D. A role for bone morphogenetic protein-4 in adipocyte development. *Cell Cycle* **6**, 385–389 (2007).
36. Kim, Y. J., Lee, M. H., Wozney, J. M., Cho, J. Y. & Ryoo, H. M. Bone morphogenetic protein-2-induced alkaline phosphatase expression is stimulated by Dlx5 and repressed by Msx2. *J. Biol. Chem.* **279**, 50773–50780 (2004).
37. Sun, P. *et al.* Loss of Lgr4 inhibits differentiation, migration and apoptosis, and promotes proliferation in bone mesenchymal stem cells. *J. Cell. Physiol.* **234**, 10855–10867 (2019).
38. Qiu, W. *et al.* Patients with high bone mass phenotype exhibit enhanced osteoblast differentiation and inhibition of adipogenesis of human mesenchymal stem cells. *J. Bone Miner. Res.* **22**, 1720–1731 (2007).
39. Taipaleenmäki, H., Abdallah, B. M., AlDahmash, A., Säämänen, A. M. & Kassem, M. Wnt signalling mediates the cross-talk between bone marrow derived pre-adipocytic and pre-osteoblastic cell populations. *Exp. Cell Res.* **317**, 745–756 (2011).
40. Liu, C. *et al.* A towering genome: Experimentally validated adaptations to high blood pressure and extreme stature in the giraffe. *Sci. Adv.* **7**, 9459–9476 (2021).
41. Baryawno, N. *et al.* A Cellular Taxonomy of the Bone Marrow Stroma in Homeostasis and Leukemia. *Cell* **177**, 1915-1932.e16 (2019).
42. Tikhonova, A. N. *et al.* The bone marrow microenvironment at single-cell resolution. *Nature* **569**, 222–228 (2019).

642 43. Dolgalev, I. & Tikhonova, A. N. Connecting the Dots: Resolving the Bone Marrow
643 Niche Heterogeneity. *Front. Cell Dev. Biol.* **9**, 478 (2021).
644 44. Pino, A. M., Miranda, M., Figueroa, C., Rodríguez, J. P. & Rosen, C. J. Qualitative
645 aspects of bone marrow adiposity in osteoporosis. *Front. Endocrinol. (Lausanne).* **7**,
646 139 (2016).
647 45. Bycroft, C. *et al.* The UK Biobank resource with deep phenotyping and genomic data.
648 *Nat. 2018 5627726* **562**, 203–209 (2018).
649 46. Van Essen, D. C. *et al.* The WU-Minn Human Connectome Project: An overview.
650 *Neuroimage* **80**, 62–79 (2013).

MATERIALS AND METHODS

Cohorts

Hangzhou Normal University (HNU) data as part of the Consortium for Reliability and Reproducibility[1]: We accessed the openly available test-retest reliability dataset from http://fcon_1000.projects.nitrc.org. In this study, T1 MRI was acquired on a 3T GE Discovery MR750 scanner using an 8-channel head coil with a repetition time of 8.06ms, 8° flip angle and 250 mm field of view at a resolution of 1x1x1 mm. We included all available data from this sample, specifically data from 30 healthy adults (50% female) aged 20-30 years (mean: 24.4, sd: 2.4 years) that were scanned ten times across one month, one scan every three days.

Human Connectome Project data[2]: We accessed openly available data from https://db.humanconnectome.org. In this study, T1 MRI was acquired on a customized 3T Siemens Skyra scanner with a repetition time of 2400ms, 8° flip angle, 224mm field of view and a voxel size of 0.7mm. We included data from 430 twins from this sample, including 174 males (60 dizygotic and 114 monozygotic, age range 22 to 34) and 256 females (96 dizygotic and 160 monozygotic, age range 26 to 36).

UK Biobank[3]: We accessed data from the UK Biobank study resource (access code 27412; https://www.ukbiobank.ac.uk). In this study, T1 MRI data was acquired on three identical 3T Siemens Skyra scanners with a repetition time of 2000ms, 8° flip angle, 256mm field of view and a resolution of 1x1x1mm. We split the available sample into a discovery set comprising 33,042 white British individuals (51% females) aged 45-82 years (mean 64.9, sd 7.5 years), and an independent replication set comprising all other individuals (N=4958, 52% female, age mean 62.9, sd 7.7, range 45-81 years). We also obtained head bone mineral density measurements produced by a DXA system (code 23226-2.0), body mass index (code 21001-2.0), and data on whether women ever used hormone-replacement therapy (code 2814-2.0). BMD data was only available for 29,093 of the samples for which MRI head scans were available.

Ethical approvals

The UK Biobank was approved by the National Health Service National Research Ethics Service (ref. 11/NW/0382). The Human Connectome Project was approved by the Washington University institutional review board. Hangzhou Normal University study protocol and data sharing was approved by its local ethics committee.

Freesurfer preprocessing and extraction of vertex intensities

We processed all T1 MRI data using the standard recon-all pipeline in Freesurfer 5.3.0. Next, we fed the intensity-normalized volumes derived via recon-all into the Freesurfer mri_watershed program to delineate the surfaces of the brain, skull and skin. We performed a stepwise extraction of intensities from layers following the shape of the outer skin, walking inward into the skull in steps of 0.5mm up to 25mm inward which produces an intensity array of length 50 for each datapoint. Since watershed delineates the skin around the entire head, we disregarded parts that are not directly on top of the cortex. For this, we identified the coordinates of the upper part of the cerebellum and the accumbens from the individual level Freesurfer aseg parcellation and defined a plane in 3D space that intersected these two points, disregarding all data points in coordinates below the plane. The resulting stream of layerwise intensities therefore comprised data on top of the cortex and was fed one-by-one into a artificial neural network model to identify and define the borders of the bone marrow (BM)

for that datapoint. See supplementary materials for more detail on this workflow, including software versions.

Intensity array data simulation

In order to train the neural network model, we generated a large synthetic dataset of intensity arrays, with known boundaries between anatomical structures, by simulating the thickness and intensity of the different structures located between the outer skin and the sub-arachnoid space. The simulation incorporated the following real-world complexities:

1. Different anatomical architectures (skin, subcutaneous fat, aponeurosis, outer table, BM, inner table, dura mater, arachnoid space), including when a structure is not present throughout the calvarium.
2. Variation in thickness and intensity between vertices (on the same calvarium)
3. A wide variety of different calvarium types with different combinations of levels of BM adiposity, bone thickness, and subcutaneous adiposity.
4. "Blurring" between anatomic structures was present in real data and was modeled in our simulations:
   a. blurring that occurred because of the voxel resolution of the MRI scanner relative to the underlying structures
   b. blurring that occurred because the layers for a data point usually do not match with voxel boundaries.

The parameters used in the simulation (primarily mean and variance of both thickness and intensity of each of the different anatomical structures within a calvarium) were estimated by reviewing the MRI scans of a wide variety of real subjects from the MRI scan collections included in this study. We simulated 336 different calvaria with the following mean characteristics: 7 BM intensities (40, 50, 70, 90, 110, 140, 170) x 6 bone thicknesses (4, 6, 8, 9, 11, 12 mm) x 8 body fat thicknesses (0, 1, 2, 3, 4, 6, 9, 12 mm) and for each calvarium we generated 5000 intensity arrays. In the iterative process of simulating data, training the network, and testing its performance on real data, we observed that incorporating the characteristics of extreme head types in the simulation parameters was critical to obtaining good performance on real data. Fine-tuning of model hyperparameters played a much lesser role. The R code and all parameters are openly available *[made public upon acceptance]* (bmSimulation_50_versionA.r)

Artificial neural network architecture and training

The network is a feed-forward fully connected network. There are 50 input nodes (for the 50 intensities of a datapoint), three internal layers with 100 nodes each (ReLU activation function), and six output nodes (upper and lower bound for each of outer table, BM, and inner table). The model was implemented in the Keras framework on top of the Tensorflow backend, and the training of the model was performed in Google Colab[4].

All vertices from all calvaria were randomly shuffled, and then two thirds of the data were used for training the model, and one third was used as the validation set, to measure the performance. The loss function, defined as the sum of the mean squared errors of the six outputs, was minimised using the Adam algorithm[5], with a learning rate of 0.1 and a batch size of 8192. We used dropout to regularise the model[6], with a 30 % dropout rate in all the hidden layers. The model is trained over 300 epochs. The performance of the network plateaus before 300 epochs (Figure S1), suggesting that the optimisation has converged on the best parameters for this model architecture.

To compute the overlap of the true and the predicted intervals, the predictions were first rounded to integers, so they refer to specific layers in the intensity vector. Then the overlap is defined as the number of layers that are included in both the predicted and the true interval, divided by the number of layers in the longest of the true and the predicted interval.

For each datapoint of a scan, we computed the mean BM intensity from the part of the intensity array predicted to be BM and then computed the mean and standard deviation across all datapoints in the scan. We did the same for the outer and inner table.

The python code is openly available *[made public upon acceptance]* (bmDetectNN50_randomAux_training_A.ipynb)

ANN Quality control measures

We performed the BM localisation procedure on the intensity data from 42,068 heads in the UK Biobank. 420 of these produced no output and 2,234 produced a calvarium with less than 5,000 vertices most likely related to poor image quality (Figure S5), leaving 39,414 samples.

We used two additional QC metrics to filter out calvaria where BM localisation was likely to have failed. First, we set an upper limit of 30 on the standard deviation of the intensity of the outer table as scans with higher values were clear outliers and were probably cases where the location of both outer table and BM has failed (Figure S6). Second, for each calvarium, we computed the Mahalonobis distance for all vertices in the two dimensions "first layer of the BM" and "BM intensity" (Figure S7). By manual inspection we found that data points with MD > 25 often had errors in BM layer identification, typically where the network had erroneously predicted a higher and more intense layer to be the BM. We considered a calvarium as failing this QC criterium if more than 0.5% of vertices have MD > 25. This criterium is very strict as errors on only 0.5% of data points in a calvarium would not significantly affect the average BM intensity for a calvarium. However, we wanted the data to be usable to generate individual calvarial BMA maps and were only willing to tolerate a very low percentage of data points with errors in each calvarium. These two additional QC filters were complementary (Figure S8) and resulted in a final number of 39,207 scans passing QC.

Twin heritability estimates

We used the monozygotic and same sex dizygotic twins from the *Human Connectome Project* dataset to fit the NACE model using the twinlm function of the mets package[7] in R (Table S1).

GWAS methods

We followed standard quality control procedures for preparing UK Biobank genetic data. Specifically, we removed individuals missing more than 1% of genotyping data, and single nucleotide polymorphisms (SNP) missing in more than 5% of individuals or with a minor allele frequency below 0.01, yielding approximately 7.9M SNPs. We split the available sample into a white British discovery set and a non-white replication set as detailed under *cohorts*. Within each of these samples, we performed sex-specific covariate regression prior to genome-wide-association analysis (GWAS). For males, we residualized our estimates of BM adiposity from age (using orthogonal polynomials of degree 2), scanning site, and the first 20 genetic principal components for population level stratification. For females, we applied the same model yet also controlling for hormonal replacement therapy as this is known to affect BMA[8] (binary: ever used HRT therapy yes/no).

The residuals were fed into GWAS using plink (version 2)[9]. Using the discovery sample, we first performed a GWAS in females only (N=16,902), and a GWAS in males only (N=16,140). After validating their significant genetic correlation (Rg=.94, P=6e-27), we performed a GWAS in the full discovery sample, merging the residuals from the female model with the residuals from the male model. Likewise, we performed a GWAS in the replication sample merging the residuals from a male and a female model in a joint GWAS (no sex-specific GWAS performed due to power in this sample). The resulting summary statistics were standardized using the python_convert toolbox (https://github.com/precimed/python_convert), removing the MHC region in chromosome 6 between base pairs 26M and 34M before feeding them into genetic correlation analysis. GWAS summary statistics are available on the FUMA website (ID XXXX) *[made public upon acceptance]*

GWAS results were post-processed using the Functional Mapping and Annotation of Genome-Wide Association Studies (FUMA) tool[11] to define genomic loci, significant independent SNPs, lead SNPs, and top lead SNPs. We used default settings which were: N = NA, Ncol = N, exMHC = 1, MHCopt = annot, extMHC = NA, ensembl = v92, genetype = protein_coding, leadP = 5e-8, gwasP = 0.05, r2 = 0.6, r2_2 = 0.1, refpanel = 1KG/Phase3, pop = EUR, MAF = 0, refSNPs = 1, mergeDist = 250. FUMA was also used to perform an eQTL analysis of the GWAS results using the GTEX v8 expression dataset. Genes, which were not the closest gene to the top lead SNP of a locus, but for which genome-wide significant SNPs were strong eQTLs, were annotated in the Manhattan plot (Figure 3).

Single-cell data and analysis

Single cell RNAseq data of BM mesenchymal lineage cells[10] was downloaded from the Single Cell Portal (https://singlecell.broadinstitute.org/single_cell/study/SCP1017) and used to create a Seurat 4.0 object in R-studio (count, embedding and meta-data). This was an integrated dataset of 7585 cells that contains endosteal Td+ BM cells from 1-month-old (1M) and 1.5-month-old (1.5M) male Col2:Td mice. We did not modify the cell clustering or nomenclature, other than excluding two chondrocyte clusters as chondrocytes originate from the resting zone progenitors, but not BM MSCs [10]. The dataset does not include lipid-laden adipocytes presumably due to the difficulty in analyzing these large and fatty cells using this method.

We searched the data from Zhong et al for the 54 genes displayed in the Manhattan plot (Figure 3). Human gene names were translated to mouse gene names and, if no similar name was identified, we searched for orthologs. For 3 of the 54 human genes, we could not identify a mouse gene and, for an additional 9 genes, the mouse gene had no expression in the scRNAseq data (Tables S7 and S8). Cluster gene expression was plotted as a dotplot (ggplot2) and patterns in gene expression were grouped by alignment to a dendrogram (ggtree) based on Euclidean distance. The expression of each gene was scaled by the gene's mean expression across clusters (i.e. cell types). Zero expression dots were removed.

GWAS downstream analysis and genetic architecture

We estimated SNP heritability and genomic inflation of the resulting GWAS summary statistics using LD-score regression[12]. The same tool was used for estimating genetic correlations with bone mineral density[13], body mass index[14], blood pressure[15] (systolic and diastolic), coronary artery disease[16], type-2 diabetes[17], multiple sclerosis[18] , Parkinson's

disease[19], Alzheimer's disease[20], general cognitive ability[21], educational attainment [22], and insomnia[23].

To estimate genetic overlap between pairs of traits we used bivariate MiXeR v1.3 (https://github.com/precimed/mixer). MiXeR[24] uses a Gaussian causal mixture model to estimate the total number of trait-influencing variants that explains 90% of SNP heritability (i.e., polygenicity). In this case, a trait-influencing variant is a common variant with a direct effect on the trait of interest excluding effects due to LD. Parameters are estimated with 20 iterations of the mixture models and the mean of each estimate is quantified along with the standard deviation over the 20 iterations. Given two traits of interest, MiXeR models the trait-influencing variants unique to each trait (non-overlapping) as well the number of shared trait-influencing variants (overlapping). To assess model fit, MiXeR employs the difference in Akaike information criterion between the MiXeR model and an infinitesimal model with a positive value indicative of good model fit.

To gain an indication of the localization of the genetic overlap between BMA and other traits, we searched for all 168 BMA independent genome-wide significant SNPs in the GWASes of the other traits. At each of the 41 loci and for each trait, we collected the number of SNPs that could be found and the number of these that were significant at 1% (Table S9).

References

1. Zuo, X. N. *et al.* An open science resource for establishing reliability and reproducibility in functional connectomics. *Sci. Data 2014 11* **1**, 1–13 (2014).
2. Van Essen, D. C. *et al.* The WU-Minn Human Connectome Project: An overview. *Neuroimage* **80**, 62–79 (2013).
3. Sudlow, C. *et al.* UK Biobank: An Open Access Resource for Identifying the Causes of a Wide Range of Complex Diseases of Middle and Old Age. *PLOS Med.* **12**, e1001779 (2015).
4. Google Colaboratory. https://colab.research.google.com/.
5. Kingma, D. P. & Ba, J. Adam: A Method for Stochastic Optimization. (2014) doi:10.48550/arxiv.1412.6980.
6. Srivastava, N., Hinton, G., Krizhevsky, A., Sutskever, I. & Salakhutdinov, R. Dropout: A Simple Way to Prevent Neural Networks from Overfitting. *J. Mach. Learn. Res.* **15**, 1929–1958 (2014).
7. Holst, K. K., Scheike, T. H. & Hjelmborg, J. B. The Liability Threshold Model for Censored Twin Data. *Comput. Stat. Data Anal.* **93**, 324–335 (2016).
8. Syed, F. A. *et al.* Effects of Estrogen Therapy on Bone Marrow Adipocytes in Postmenopausal Osteoporotic Women. *Osteoporos. Int.* **19**, 1323 (2008).
9. Purcell, S. *et al.* PLINK: A Tool Set for Whole-Genome Association and Population-Based Linkage Analyses. *Am. J. Hum. Genet.* **81**, 559 (2007).
10. Zhong, L. *et al.* Single cell transcriptomics identifies a unique adipose lineage cell population that regulates bone marrow environment. *Elife* **9**, (2020).
11. Watanabe, K., Taskesen, E., Van Bochoven, A. & Posthuma, D. Functional mapping and annotation of genetic associations with FUMA. *Nat. Commun. 2017 81* **8**, 1–11 (2017).
12. Bulik-Sullivan, B. *et al.* LD Score regression distinguishes confounding from polygenicity in genome-wide association studies. *Nat. Genet. 2015 473* **47**, 291–295 (2015).
13. Morris, J. A. *et al.* An atlas of genetic influences on osteoporosis in humans and mice.

Nat. Genet. **51**, 258–266 (2019).

14. Yengo, L. *et al.* Meta-analysis of genome-wide association studies for height and body mass index in ~700000 individuals of European ancestry. *Hum. Mol. Genet.* **27**, 3641–3649 (2018).
15. Evangelou, E. *et al.* Genetic analysis of over 1 million people identifies 535 new loci associated with blood pressure traits. *Nat. Genet. 2018 5010* **50**, 1412–1425 (2018).
16. Nikpay, M. *et al.* A comprehensive 1000 Genomes–based genome-wide association meta-analysis of coronary artery disease. *Nat. Genet. 2015 4710* **47**, 1121–1130 (2015).
17. Mahajan, A. *et al.* Fine-mapping type 2 diabetes loci to single-variant resolution using high-density imputation and islet-specific epigenome maps. *Nat. Genet. 2018 5011* **50**, 1505–1513 (2018).
18. Patsopoulos, N. A. *et al.* Multiple sclerosis genomic map implicates peripheral immune cells and microglia in susceptibility. *Science (80-.).* **365**, (2019).
19. Nalls, M. A. *et al.* Identification of novel risk loci, causal insights, and heritable risk for Parkinson's disease: a meta-analysis of genome-wide association studies. *Lancet Neurol.* **18**, 1091–1102 (2019).
20. Wightman, D. P. *et al.* A genome-wide association study with 1,126,563 individuals identifies new risk loci for Alzheimer's disease. *Nat. Genet.* **53**, 1276–1282 (2021).
21. Savage, J. E. *et al.* Genome-wide association meta-analysis in 269,867 individuals identifies new genetic and functional links to intelligence. *Nat. Genet. 2018 507* **50**, 912–919 (2018).
22. Lee, J. J. *et al.* Gene discovery and polygenic prediction from a genome-wide association study of educational attainment in 1.1 million individuals. *Nat. Genet. 2018 508* **50**, 1112–1121 (2018).
23. Jansen, P. R. *et al.* Genome-wide analysis of insomnia in 1,331,010 individuals identifies new risk loci and functional pathways. *Nat. Genet. 2019 513* **51**, 394–403 (2019).
24. Frei, O. *et al.* Bivariate causal mixture model quantifies polygenic overlap between complex traits beyond genetic correlation. *Nat. Commun. 2019 101* **10**, 1–11 (2019).